

The Debris Disk of Solar Analogue τ Ceti: *Herschel* Observations and Dynamical Simulations of the Proposed Multiplanet System

S. M. Lawler^{*1,2}, J. Di Francesco^{2,1}, G. M. Kennedy³, B. Sibthorpe⁴, M. Booth⁵, B. Vandenbussche⁶, B. C. Matthews^{2,1}, W. S. Holland^{7,8}, J. Greaves⁹, D. J. Wilner¹⁰, M. Tuomi^{11,12}, J. A. D. L. Blommaert^{13,14,6}, B. L. de Vries^{15,16}, C. Dominik^{17,18}, M. Fridlund^{19,20}, W. Gear²¹, A. M. Heras²², R. Ivison^{23,24}, G. Olofsson¹⁵

¹Department of Physics & Astronomy, University of Victoria, PO Box 1700, STN CSC, Victoria, BC V8W 2Y2, Canada

²National Research Council of Canada, Herzberg Astronomy & Astrophysics Program, 5071 West Saanich Road., Victoria, BC V9E 2E7, Canada

³Institute of Astronomy, Cambridge University, Madingley Road, Cambridge CB3 0HA, UK

⁴SRON Netherlands Institute for Space Research, 9747 AD, Groningen, The Netherlands

⁵Instituto de Astrofísica, Pontificia Universidad Católica de Chile, Vicuña Mackenna 4860, 7820436 Macul, Santiago, Chile

⁶Institute of Astronomy KU Leuven, Celestijnenlaan 200D, 3001 Leuven, Belgium

⁷UK Astronomy Technology Centre, Royal Observatory Edinburgh, Blackford Hill, Edinburgh EH9 3HJ, UK

⁸Institute for Astronomy, University of Edinburgh, Royal Observatory Edinburgh, Blackford Hill, Edinburgh EH9 3HJ, UK

⁹SUPA, School of Physics and Astronomy, University of St. Andrews, North Haugh, St. Andrews KY16 9SS, UK

¹⁰Harvard-Smithsonian Center for Astrophysics, 60 Garden Street, Cambridge, MA 02138, USA

¹¹Centre for Astrophysics Research, University of Hertfordshire, College Lane, AL10 9AB, Hatfield, UK

¹²Departamento de Astronomía, Universidad de Chile, Camino del Observatorio 1515, Las Condes, Santiago, Chile

¹³Astronomy and Astrophysics Research Group, Department of Physics and Astrophysics, Vrije Universiteit Brussel, Pleinlaan 2, 1050 Brussels, Belgium

¹⁴Flemish Institute for Technological Research (VITO), Boeretang 200, 2400 Mol, Belgium

¹⁵Department of Astronomy, Stockholm University, AlbaNova University Center, 10691 Stockholm, Sweden

¹⁶Stockholm University Astrobiology Centre, SE-106 91 Stockholm, Sweden

¹⁷Anton Pannekoek Institute, University of Amsterdam, Science Park 904, 1098 XH Amsterdam, The Netherlands

¹⁸Department of Astrophysics/IMAPP, Radboud University Nijmegen, PO Box 9010, NL-6500 GL Nijmegen, The Netherlands

¹⁹Institute of Planetary Research, German Aerospace Center, Rutherfordstrasse 2, 124 89, Berlin, Germany

²⁰Leiden Observatory, University of Leiden, PO Box 9513, 2300 RA, Leiden, The Netherlands

²¹School of Physics and Astronomy, Cardiff University, Queens Buildings, The Parade, Cardiff CF24 3AA, UK

²²Scientific Support Office, Science and Robotic Exploration Directorate, ESA/ESTEC, Keplerlaan 1, 2200 AG Noordwijk, The Netherlands

²³European Southern Observatory, Karl Schwarzschild Strasse 2, D-85748 Garching, Germany

²⁴Institute for Astronomy, University of Edinburgh, Blackford Hill, Edinburgh EH9 3HJ, UK

Released 2014 Xxxxx XX

ABSTRACT

τ Ceti is a nearby, mature G-type star very similar to our Sun, with a massive Kuiper Belt analogue (Greaves et al. 2004) and possible multiplanet system (Tuomi et al. 2013) that has been compared to our Solar System. We present *Herschel Space Observatory* images of the debris disk, finding the disk is resolved at 70 μm and 160 μm , and marginally resolved at 250 μm . The *Herschel* images and infrared photometry from the literature are best modelled using a wide dust annulus with an inner edge between 1–10 AU and an outer edge at ~ 55 AU, inclined from face-on by $35^\circ \pm 10^\circ$, and with no significant azimuthal structure. We model the proposed tightly-packed planetary system of five super-Earths and find that the innermost dynamically stable disk orbits are consistent with the inner edge found by the observations. The photometric modelling, however, cannot rule out a disk inner edge as close to the star as 1 AU, though larger distances produce a better fit to the data. Dynamical modelling shows that the 5 planet system is stable with the addition of a Neptune or smaller mass planet on an orbit outside 5 AU, where the Tuomi et al. analysis would not have detected a planet of this mass.

Key words: circumstellar matter – planet-disc interactions – planets and satellites: dynamical evolution and stability – stars: individual: τ Ceti

1 INTRODUCTION

Although hundreds of planetary systems are now known, we are still trying to understand whether or not our Solar System is typical. The distributions of known planetary system parameters are strongly affected by observational biases that are not easy to disentangle from the true distributions. Moreover, our Solar System’s architecture (small rocky inner planets, large gaseous outer planets, and an outer debris disk) has not yet been found in other systems, most likely due to these same biases. For example, long time baselines are required to discover planets at greater than a few AU by either the transit or radial velocity (RV) techniques, and directly imaging planets around mature stars like τ Ceti (5.8 Gyr; Mamajek & Hillenbrand 2008), is difficult due to the low fluxes of planets after they lose most of their initial heat from formation (e.g. Spiegel & Burrows 2012).

Fortunately, structures in debris disks can indicate the presence of additional planets. Indeed, one planet so far has been predicted based on disk morphology and then later discovered by direct imaging or another technique, (β Pic b Mouillet et al. 1997; Lagrange et al. 2010). In this paper, we use the debris disk to probe the planetary system around τ Ceti.

τ Ceti is a solar-type analogue located only 3.65 pc from the Sun. The infrared excess toward τ Ceti has been known for nearly three decades, first discovered by IRAS (Aumann 1985) and later confirmed by ISO (Habing et al. 2001).

Greaves et al. (2004), using the Submillimeter Common-User Bolometer Array (SCUBA; Holland et al. 1999) instrument on the James Clerk Maxwell Telescope (JCMT), found τ Ceti to have a significant excess and moderately resolved disk at 850 μm , extending 55 AU from the star, and inferred to be misaligned with the rotational axis of the star. They fit the observed excess between 60 μm and 850 μm with a single temperature blackbody at 60 K, and obtained a disk mass of 1.2 M_{\oplus} , about an order of magnitude higher than our Kuiper Belt.

Here, we revisit the τ Ceti disk with higher-resolution far-IR images taken by the *Herschel Space Observatory*¹, attempting to better constrain the properties of the disk. Additionally, we find the observed disk probably does not overlap with the orbits of the proposed multiplanet system (Tuomi et al. 2013), though we cannot rule out a disk inner edge inside the orbit of the outermost planet.

In Section 2, we present the *Herschel* observations. Section 3 discusses the constraints these observations place on the properties of the τ Ceti debris disk. In Section 4, we show that the disk inner edge inferred from the modelling is compatible with the proposed compact multiplanet system, and we use dynamical simulations to investigate system stability and the possible presence of additional planets. In Section 5 we discuss the τ Ceti disk-planet system in the context of other known solar

Table 1. *Herschel* Observations of τ Ceti

ObsID	Date	Instrument	Duration (s)
1342199389	2010 June 29	SPIRE 250/350/500	2906
1342213575	2011 January 31	PACS 70/160	5478
1342213576	2011 January 31	PACS 70/160	5478

Table 2. *Herschel* Measurements of τ Ceti

λ (μm)	Flux (mJy)	Unc. (mJy)	Beam size ($''$)
70	303	6	5.6
160	111	8	11.3
250	35	10	18.1
350	<28	-	25.2
500	<20	-	36.9

systems, and a summary of our conclusions is given in Section 6.

2 HERSCHEL OBSERVATIONS

τ Ceti and its surroundings were observed with the *Herschel Space Observatory* (Pilbratt et al. 2010) using both the Photodetector Array Camera and Spectrometer (PACS; Poglitsch et al. 2010) and the Spectral and Photometric Imaging Receiver (SPIRE; Griffin et al. 2010) as part of the Guaranteed Time Key Programme “Stellar Disk Evolution” to study the six most well-known debris disks (PI: G. Olofsson; Proposal ID: KPGT_golofs01.1). Data at 70 μm and 160 μm were obtained simultaneously using the PACS large scan-map mode on 31 January 2011 over a successive scan and a cross-scan each lasting 91.3 minutes (ObsIDs: 1342213575 and 1342213576). The PACS scan speed was 20'' s⁻¹. Data at 250 μm , 350 μm , and 500 μm were obtained simultaneously in the SPIRE large photometric scanning observing mode (“SpirePhotoLargeScan”) on 29 June 2010 over one pass lasting 48.4 minutes (ObsID: 1342199389). The SPIRE scan speed was 30'' s⁻¹ (the medium scan rate). Table 1 summarizes the *Herschel* observations.

The PACS and SPIRE data were reduced separately following standard procedures in HIPE version 13 (Ott 2010) using calibration set 65. Table 2 lists the measured fluxes or upper limits for each band. PACS aperture photometry is measured using 12'' and 22'' apertures for the 70 and 160 μm bands, respectively. Uncertainties for the PACS photometry values are computed using several apertures on the background. All uncertainties are 1 σ . Table 2 also lists the beam sizes for each band (Vandenbussche et al. 2010).

The SPIRE data provide mainly upper limits, as the disk grows fainter and the resolution grows larger as we proceed to longer wavelengths. At 250 μm , assuming the disk is not resolved, the flux comes from the peak pixel, which has 24 ± 6 mJy, with the uncertainty coming from confusion. Using the modelling described in Section 3.1.1, we find 35 ± 10 mJy. This is more reliable since the disk may be marginally resolved at 250 μm . At 350 μm there

¹ *Herschel* is an ESA space observatory with science instruments provided by European-led Principal Investigator consortia and with important participation from NASA.

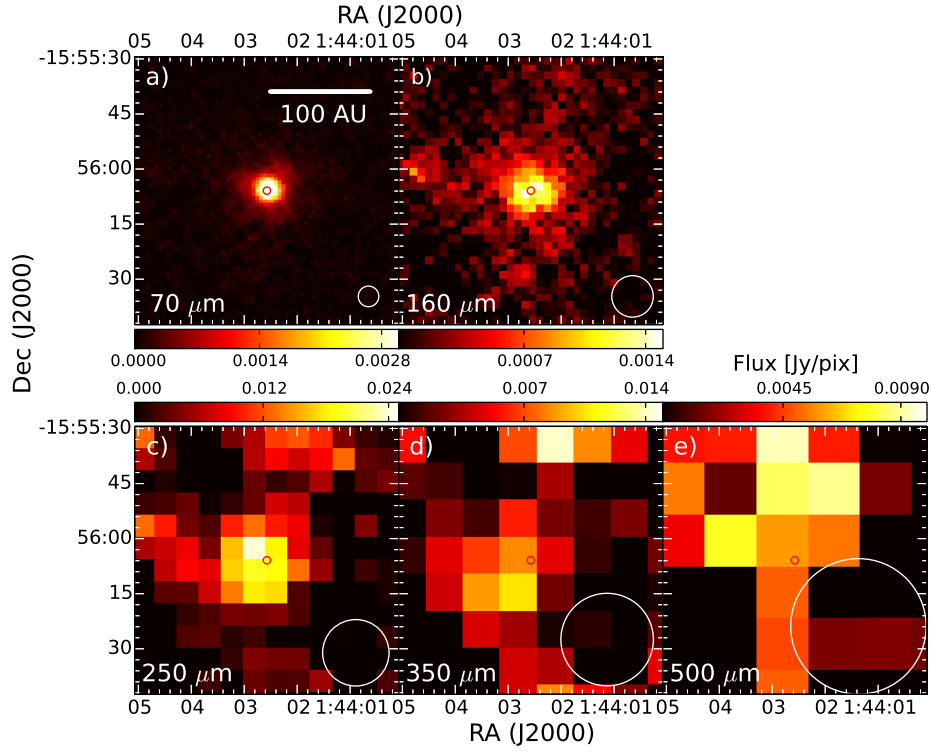


Figure 1. Cropped *Herschel* maps of τ Ceti centered on the position of peak 70 μm emission (shown in each panel as a small red circle). Beam size at each wavelength is shown for reference in each panel (larger white circles). A scalebar showing the color range of flux in Jy per pixel is shown above each sub-figure. a) 70 μm emission, b) 160 μm emission, c) 250 μm emission, d) 350 μm emission, and e) 500 μm emission. A bar in a) shows the spatial extent of 100 AU at the distance of τ Ceti.

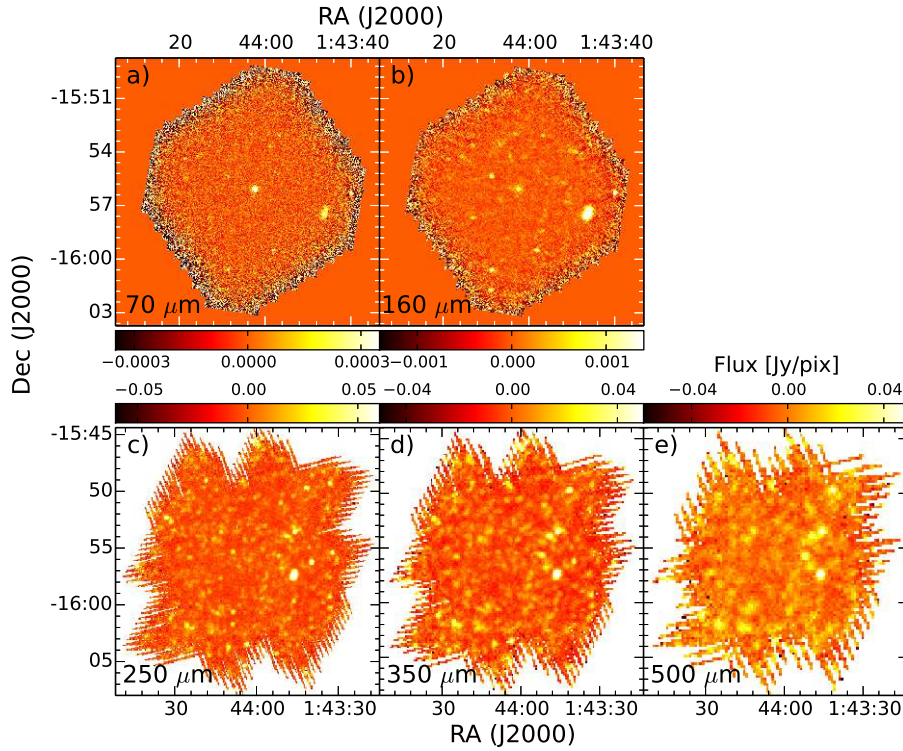


Figure 2. Uncropped *Herschel* maps of the τ Ceti region. A scalebar showing the color range of flux in Jy per pixel is shown above each sub-figure a) 70 μm emission, b) 160 μm emission, c) 250 μm emission, d) 350 μm emission, and e) 500 μm emission.

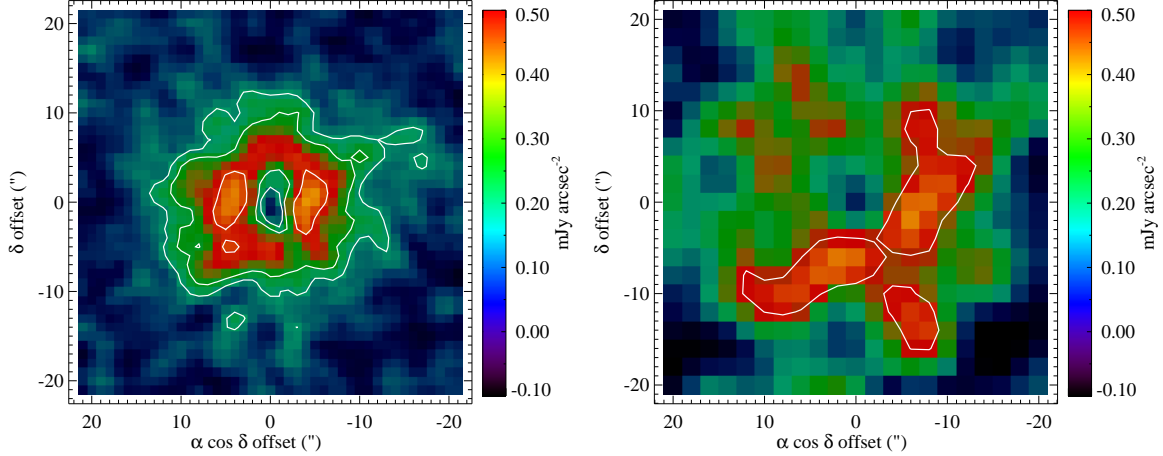


Figure 3. Peak-subtracted images at 70 (left) and 160 μm (right). Here a PSF has been scaled to the flux of the peak pixel in each band and subtracted from the images (see text for details). Contours show 3 σ , 5 σ , and 10 σ significance levels of the remaining flux (only the 3 σ contour is visible in the right image).

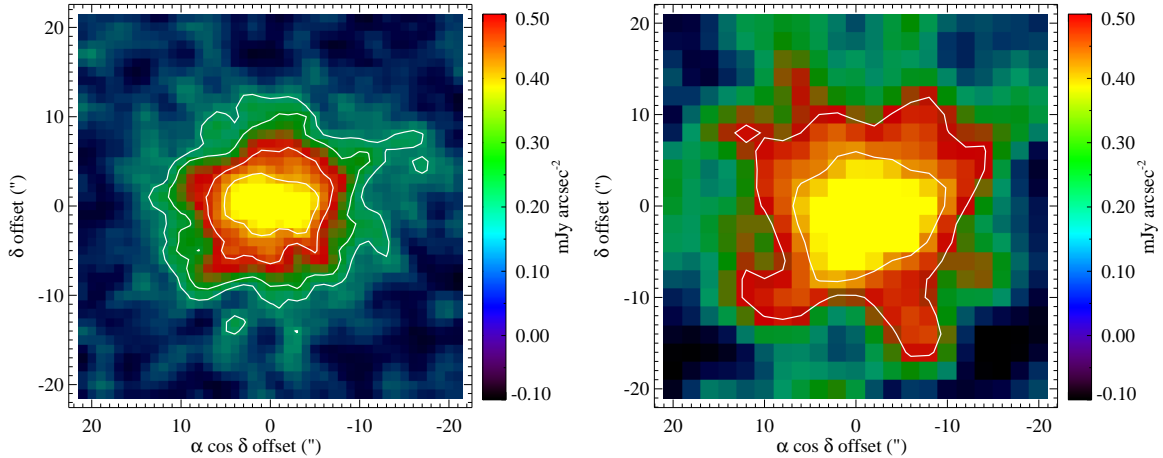


Figure 4. Star-subtracted images at 70 (left) and 160 μm (right). Here a PSF has been scaled to the photospheric flux in each band and subtracted from the images. Contours show 3 σ , 5 σ , 10 σ , and 15 σ significance levels of the remaining flux (only the 3 σ and 5 σ contours are visible in the right image).

is some emission where τ Ceti is expected to be, which added to the confusion limit gives <28 mJy. At 500 μm , only confusion is visible, giving a limit of <20 mJy.

Photometric calibration uncertainties are expected to be within 3% at 70 μm , 5% at 160 μm , and 15% at 250 μm , 350 μm , and 500 μm (Poglitsch et al. 2010; Swinyard et al. 2010; Müller et al. 2011).

Figure 1 shows a composite of cropped *Herschel* maps at 70 μm , 160 μm , 250 μm , 350 μm , and 500 μm , centered at a position of 01:44:02.6, -15:56:05.8 (J2000), the position of peak emission at 70 μm . This position is within $\sim 1''$ of the expected position of τ Ceti, given both its ICRS coordinates (i.e., 01:44:04.08, -15:56:14.9) and proper motion ($\mu_\alpha = -1.72105'' \text{ yr}^{-1}$, $\mu_\delta = +0.85416'' \text{ yr}^{-1}$) from the Hipparcos Catalogue (van Leeuwen 2007).

τ Ceti at 70 μm in Figure 1a is bright and quite compact; the three “lobes” located in the NNW, SSW, and ENE directions are artifacts of the PACS beam at

70 μm . Given these secondary beam features, it is not possible to tell by eye if any 70 μm emission is extended. The source at 160 μm in Figure 1b is less bright but still compact. At 250 μm (see Figure 1c), the source is less significant but the star-centered emission is associated with τ Ceti. At 350 μm and 500 μm (Figures 1d and 1e respectively), any emission at the τ Ceti position is hard to distinguish from the background confusion.

Figure 2 shows the uncropped *Herschel* maps at each wavelength, stretched in colour to emphasize faint background sources. At 70 μm (Figure 2a), τ Ceti dominates the image but a few other background sources are seen. Most notably, the extended galaxy MCG-03-05-018 located to the WSW at 01:43:46.8, -15:57:29 (J2000) is also detected. Moving to 160 μm (Figure 2b), τ Ceti is no longer the brightest object seen; MCG-03-05-018 and many other background objects are brighter. Also, more faint background sources are seen. At 250 μm , 350 μm ,

and $500\ \mu\text{m}$ (Figures 2c, d, and e, respectively), though some emission may be associated with τ Ceti (particularly at $250\ \mu\text{m}$), it is barely distinguishable from emission of background objects. Note that MCG-03-05-018 is clearly detected in all five *Herschel* bands.

3 τ CETI'S DEBRIS DISK

It is not obvious from Figure 1 that a disk is present due to large contrast with the star. Therefore, we present peak- and star-subtracted images to highlight the extended disk structure. Figure 3 shows the images of the flux toward τ Ceti at 70 and $160\ \mu\text{m}$, where the point-spread function (PSF) has been scaled to the value of the peak pixel and subtracted. This makes it clear that there is extended structure around τ Ceti, visible at both 70 and $160\ \mu\text{m}$. For comparison, Figure 4 shows the star-subtracted images at the same wavelengths, where the PSF has been scaled to τ Ceti's photosphere and subtracted; contours give significance of the remaining flux.

Figure 5 shows the observed flux density distribution (hereafter referred to as spectral energy distribution; SED) of τ Ceti, using data obtained from the literature and *Herschel* (see caption and Table 3 for specific references). Figure 5 also shows a stellar photosphere model fit to the data. As can be easily seen, the stellar model fits the data from optical to mid-infrared wavelengths ($24\ \mu\text{m}$). At longer (PACS) wavelengths, however, the observed fluxes are significantly higher than those expected from the photosphere alone. For example, the observed $160\ \mu\text{m}$ flux is $111 \pm 8\ \text{mJy}$ while the expected $160\ \mu\text{m}$ flux from the photosphere is $31.1 \pm 0.4\ \text{mJy}$.

The appearance of excess emission in the SED suggests that τ Ceti is indeed surrounded by cooler dust. The narrow wavelength range of the detected excess and the lack of widely extended PACS emission, however, put constraints on the location of this dust. On one hand, the fact that the excess is seen only at wavelengths longer than $24\ \mu\text{m}$ suggests the dust is cold and thus situated at relatively large distances from the star. On the other hand, the small scale of the emission in the PACS images suggests the dust also cannot be too far from the star. In the following, we describe a simple debris disk model that remains consistent with the observed optical to mid-infrared emission, and that also can reproduce well the fluxes and extents of the observed far-infrared (PACS) emission.

3.1 Modelling the Disk

We modelled the τ Ceti disk images and spectrum in a two-step process. The images provide all-important constraints on the spatial structure, which we obtain first by reproducing the PACS and SPIRE $250\ \mu\text{m}$ images using a simple dust disk model (Section 3.1.1). This process does not yield definitive results because the PACS image resolutions limit what can be inferred about the disk inner edge. Using the results from the spatial modelling and an additional assumption of specific grain properties to model the disk spectrum (Section 3.1.2) yields further constraints on the disk inner edge.

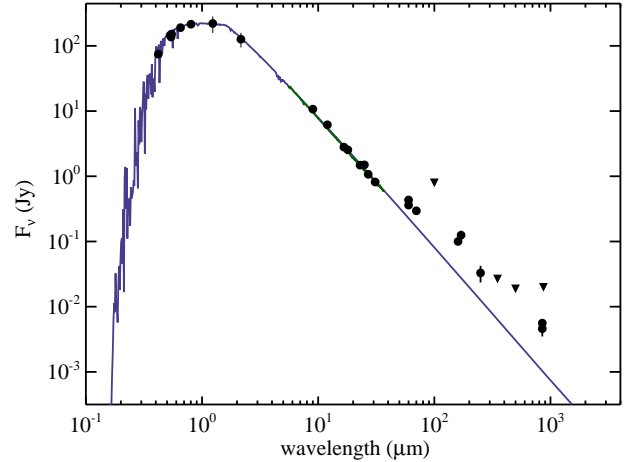


Figure 5. Observed SED of τ Ceti. Circles are measured fluxes, while triangles show upper limits. *Spitzer* IRS data are shown in green, on top of the photospheric model (blue line). The observed data include fluxes obtained from optical (Merrilliod 2006; Høg et al. 2000; Hauck & Merrilliod 1998; Perryman & ESA 1997; Bessel 1990), 2MASS (Skrutskie et al. 2006), *Spitzer* (Chen et al. 2006), AKARI (Ishihara et al. 2010), IRAS (Moshir 1990), ISO (Habing et al. 2001), JCMT (Greaves et al. 2004, Greaves et al. in prep.), and HHT (Holmes et al. 2003), as well as the *Herschel* PACS and SPIRE values and upper limits. See Tables 2 and 3 for values.

3.1.1 Image-Based Disk Model

We first use the PACS and SPIRE $250\ \mu\text{m}$ images to fit a physical model for the disk structure. The $250\ \mu\text{m}$ image has little spatial information, but we can measure the model flux as a check on the above photometry (finding $35 \pm 10\ \text{mJy}$, larger than the $24\ \text{mJy}$ estimated above if the disk were unresolved at $250\ \mu\text{m}$). Our spatial model has been used previously to model *Herschel*-resolved debris disks (e.g. Kennedy et al. 2012, 2013), and generates a high-resolution image of an azimuthally symmetric dust distribution with a small opening angle, as viewed from a specific direction. These models are then convolved with a point spread function model (observations of calibration star α Tau) for comparison with the observed disk (Figure 6). The best-fitting model is found using by-eye approximation followed by least-squares minimization. As the entire multi-dimensional parameter space was not searched, the model presented is not necessarily unique, but provides a good indication of the probable disk structure. By checking the fit of different parameter combinations, we were able to get a good feel for how well-constrained the different parameters are and feel we have converged on a good model, within observational errors.

Due to the limited resolution of the images of τ Ceti, our model disk is a simple power-law in radial surface density ($\Sigma \propto r^\gamma$), which extends from r_{in} to r_{out} . This approach allows us to test whether or not the disk is radially extended. We use the simple assumption of a blackbody temperature law ($T = T_{1\text{AU}} r^{-0.5}$, with $T_{1\text{AU}}$ being the disk temperature at 1 AU and radius r in AU). Given that the disk temperature and surface density are degenerate without multiple well-resolved images, neither

Table 3. Observational Data from the Literature

Band	λ (μm)	Obs. Flux (Jy)	Uncertainty (Jy)	Citation
U_J	0.364	146.6	3.2	Mermilliod (2006)
B_T	0.42	74.7	1.1	Høg et al. (2000)
B_J	0.442	146.4	3.2	Mermilliod (2006)
V_T	0.532	145.7	1.4	Høg et al. (2000)
H_p	0.541	136.7	0.68	Perryman & ESA (1997)
V_J	0.547	151.9	3.2	Mermilliod (2006)
R_C	0.653	190.2	3.5	Bessel (1990)
I_C	0.803	214.9	3.9	Bessel (1990)
J	1.24	220.6	63	Cutri et al. (2003)
K_s	2.16	126.4	32	Cutri et al. (2003)
IRS1 ^a	6.5	18.15	0.65	Chen et al. (2006)
IRS2 ^a	8.69	10.19	0.24	Chen et al. (2006)
AKARI9	9	10.71	0.17	Ishihara et al. (2010)
IRS3 ^a	11.4	5.885	0.13	Chen et al. (2006)
IRAS12	12	6.158	0.42	Moshir (1990)
IRS4 ^a	16.6	2.801	0.073	Chen et al. (2006)
AKARI18	18	2.544	0.071	Ishihara et al. (2010)
IRS5 ^a	22.9	1.509	0.039	Chen et al. (2006)
IRAS25	25	1.503	0.14	Moshir (1990)
IRS6 ^a	27	1.094	0.025	Chen et al. (2006)
IRS7 ^a	31	0.8393	0.021	Chen et al. (2006)
ISO60	60	0.433	0.037	Habing et al. (2001)
IRAS60	60	0.3978	0.048	Moshir (1990)
IRAS100	100	0.8253	0.27	Moshir (1990)
ISO170	170	0.125	0.021	Habing et al. (2001)
SCUBA	850	0.0058	0.0006	Greaves et al. (2004)
SCUBA-2	850	0.005	0.001	Greaves et al. (in prep.)
HHT870	870	<0.0198	-	Holmes et al. (2003)

^a IRS values are binned from spectral data in Chen et al. (2006).

γ nor $T_{1\text{AU}}$ is well constrained. Physically, $T_{1\text{AU}}$ should be greater than about 230 K, because this is the temperature that grains with blackbody absorption and emission would have at 1 AU from τ Ceti. Temperatures up to factors of 3-4 greater are possible if the emission comes primarily from small grains, which emit inefficiently at long wavelengths and have higher temperatures to maintain energy equilibrium (e.g. Booth et al. 2013).

The model also includes a background source to the east that is only visible in the 160 μm image. This does not significantly affect any of the parameters of the fit, but does allow us to better estimate the 250 μm disk flux.

To model the *Herschel* images of τ Ceti, we initially tried a simple narrow ring. We found that this model failed to reproduce the observed images and conclude that the emission is radially extended. We therefore allowed r_{in} and r_{out} , and γ , the surface density power-law exponent, to vary independently. The low surface brightness of the disk in the *Herschel* images limits our ability to constrain the disk model parameters. Primarily, a degeneracy between disk surface density profile, the inner edge location, and the dust temperature allowed a range of models to reproduce the data. For a $\gamma = -1$ model, the disk is centrally concentrated and the best fitting inner edge is at about 10 AU with $T_{1\text{AU}} \sim 380$ K. For a flat profile ($\gamma = 0$) the disk is less centrally concentrated and the inner edge is closer, around 2 AU (and $T_{1\text{AU}}$ is the same). For a radially increasing surface density ($\gamma = 1$),

the inner edge is around 3 AU and $T_{1\text{AU}} \sim 180$ K. We return to this issue when considering SED models that make assumptions about grain properties in section 3.1.2 below.

The low surface brightness of the disk in the *Herschel* images limits our ability to constrain the disk model parameters. However, despite the degeneracies between $T_{1\text{AU}}$, r_{in} and γ , the best fitting models have similar inner radii of 2-3 AU (with large uncertainty, acceptable fits range from roughly 1-10 AU), and outer radii of 55 AU \pm 5 AU. The disk may however extend to larger radii at a level undetectable by these observations. The disk geometry is constant across different models, with a disk inclination (i.e., from face-on) of 35° and position angle (East of North) of 105°. Using brute-force grid calculations we estimate that the 1σ uncertainty in these angles is about 10°.

Figure 6 shows an example of a well fitting model with $\gamma = 0$. Some residual structure is seen near the star at 70 μm , and very similar structure is seen for different models. We suspect it arises due to the brightness of τ Ceti itself; the high signal-to-noise ratio of the stellar emission means that the PSF model used (α Tau) must be a very good match to the PSF for the τ Ceti observation. Kennedy et al. (2012) showed that the PACS 70 μm PSF varies at the 10% level, which is a probable reason for the non-zero residuals near the star.

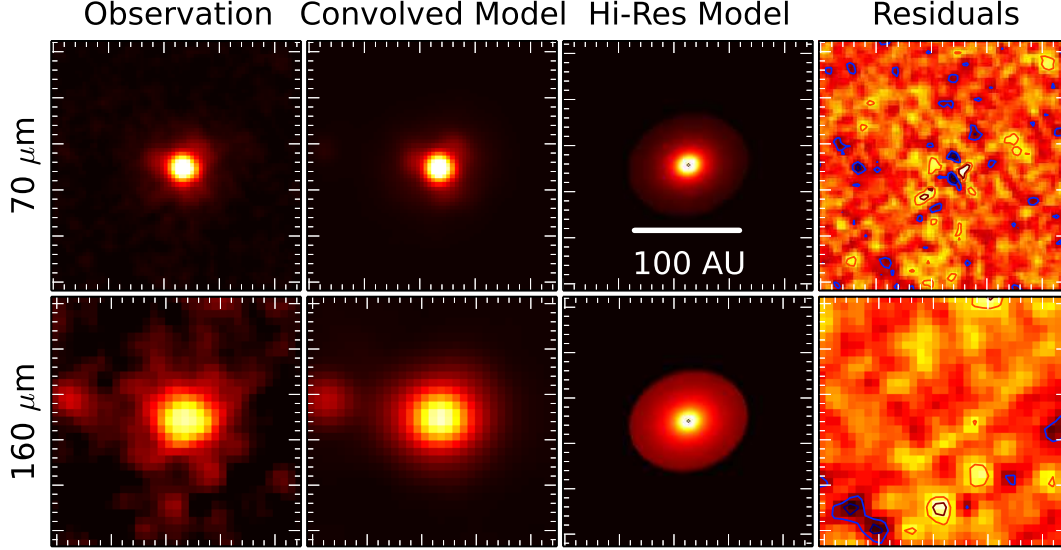


Figure 6. An example of a disk model that matches the *Herschel* images. Panels are on the same scale as Figure 1, and a 100 AU scale bar is shown for reference. Top panels show the *Herschel* data and model at 70 μm , lower panels at 160 μm . From left to right, panels show the *Herschel* data, the model convolved to the same resolution as the data, a high resolution version of the model, and the residuals of data-model (-3σ , -2σ , 2σ , and 3σ contours). Some 3σ residuals are still visible in the 70 μm image; these are probably due to imperfect fitting of the beam (see text).

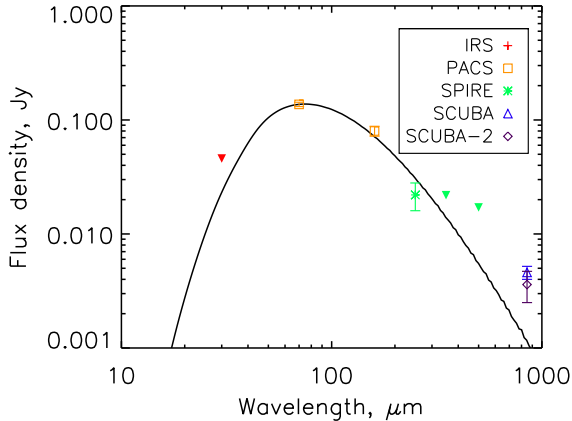


Figure 7. Fitting the SED with a realistic grain model, using a flat surface density profile ($\gamma = 0$). The *Herschel* PACS and SPIRE 250 μm datapoints are used in the fit, along with upper limits from *Spitzer* IRS and *Herschel* SPIRE 350 μm and 500 μm . SCUBA and SCUBA-2 850 μm data are also shown, but are not used in the fit. See legend for symbols.

3.1.2 SED-Based Disk Model

Though in general the shape of a modified blackbody provides a good approximation to the emission profile of dust grains, it cannot tell us much about the properties of the grains. A better approximation of the dust grains can be found by taking into account their optical properties and the size distribution of dust in the disk. Accordingly, we follow the model described in Wyatt & Dent

(2002) and similarly assume non-porous, amorphous silicate grains with an organic refractory mantle. The silicate core makes up 1/3 of the grains, which have an amorphous carbon coating. Grains are assumed to be spherical, and absorption efficiencies are calculated using Mie theory, Rayleigh-Gans theory, or geometric optics in the appropriate limits (see also Li & Greenberg 1997). We assume these grains follow a size distribution power law of $n(D)dD \propto D^{-3.5}dD$ from a minimum grain size, D_{\min} , to an arbitrarily large grain size (Dohnanyi 1969). Many of the properties of the grain model are degenerate. For instance, a shallower size distribution has the same effect as increasing the minimum grain size, and the exact composition of the grains cannot easily be determined without spectral features. For this reason, we only varied D_{\min} and the inner edge of the disk (since this was poorly constrained from the image-based modelling). We also tested two values of the surface density power law, γ equal to 0 and 1 since this quantity is also poorly constrained from the image-based modelling.

No SED model can be found that fits both the SCUBA and PACS 160 μm photometry, suggesting that a separate, cooler disk component may be required to fully explain the sub-mm observations, since a slope that fits both these points is too shallow to even be fit by a perfect blackbody. Further investigation of the multi-epoch SCUBA and SCUBA-2 data is left to Greaves et al. (in prep).

For the following we therefore focus on fitting the model to the PACS data, the SPIRE data and the upper limit from the *Spitzer* IRS spectral data. We find the best fitting model to have a flat surface density profile ($\gamma = 0$), a minimum grain diameter of $15 \pm 8 \mu\text{m}$ and an inner

radius of 6_{-4}^{+15} AU (parameter uncertainties calculated using a χ^2 cut). The best fit is shown in Figure 7. There is some anti-correlation between the minimum diameter and inner radius such that models with a larger inner radius require a smaller minimum grain size. Models with a rising surface density of $\gamma = 1$ can still plausibly fit the photometry with a minimum grain size of $8 \mu\text{m}$ and an inner radius between 1 AU and 17 AU, although this provides a poorer fit to the data.

Unfortunately, these SED models were not very sensitive to different disk inner edges, and the results of this modeling technique, while agreeing with the results of the image-based model, did not provide any stronger constraints on the inner edge of the disk.

3.1.3 Disk Properties Inferred from Both Models

To summarize the findings of both models, τ Ceti's disk extends from a radius similar to the inner Solar System (~ 1 -10 AU) to just outside the distances inhabited by the main classical Kuiper Belt.

The image-based model's uncertainty in the inner edge locations arises from the variations in the $70 \mu\text{m}$ beam shape and the resolution limits in both PACS wavelengths. The uncertainty in the inner edge as predicted by the SED-based model can be attributed to the calibration uncertainties in the *Spitzer* IRS spectrum and a small number of photometric measurements of the excess, while the outer edge uncertainty is mainly due to the low surface brightness in the PACS $160 \mu\text{m}$ image.

We do not give a mass estimate for our dust models, as the uncertainties due to assumptions about the grains give disk masses that vary by orders of magnitude. The most accurate disk masses come from submillimeter fluxes, temperatures, and opacities, thus we leave calculation of the disk mass in the τ Ceti system to the forthcoming SCUBA and SCUBA-2 analysis (Greaves et al. in prep.)

In the next section, we will use the (limited) constraints imposed by the disk to investigate the validity of a proposed planetary system.

4 τ CETI'S POSSIBLE PLANETARY SYSTEM

Though previous studies failed to find planets around τ Ceti using the radial velocity technique (e.g. Pepe et al. 2011), Tuomi et al. (2013) report evidence for a five planet system after extensive modelling and Bayesian statistical analysis using combined radial velocity data from three different planet surveys.

The most likely system found by Tuomi et al. consists of five super-Earths, ranging in mass ($M \sin i$) from 2.0-6.6 M_{\oplus} , with small-to-moderate eccentricities (~ 0 -0.2), in a tightly-packed configuration with semimajor axes ranging from 0.105-1.35 AU. Tuomi et al. (2013) show that their system is stable based on Lagrange stability thresholds, but do not perform detailed numerical integrations.

We note that the periodic RV signals detected by Tuomi et al. (2013) were only interpreted as planets by

Table 4. Properties of a Stable Planet System around τ Ceti

planet	M^a (M_{\oplus})	a (AU)	e
a	4.0	0.105	0.16
b	6.2	0.195	0.03
c	7.2	0.374	0.08
d	8.6	0.552	0.05
e	13.2	1.35	0.03

^a Planet masses are given assuming $i_{\text{sys}} = 30^\circ$

these authors with caution; it is possible that the signals are from another source, such as stellar activity or instrumental bias, although there is no direct evidence in favour of these alternative interpretations either. In this section we investigate the stability of the proposed planet system, and assuming that the planetary system is real, use it to place constraints on the inner disk edge using dynamical simulations.

4.1 System Inclination

Since the planets' existence was surmised using RV data, we have no direct information on the inclination of the planetary system. In addition to the coplanar precedent of our own Solar System, several recent studies find evidence that star-planet-disk systems without hot Jupiters should be well-aligned. For example, Kennedy et al. (2013) discuss the HD 82943 system, where the star, planets, and debris disk have well-measured inclinations, and are all coplanar within $\sim 10^\circ$. Furthermore, Greaves et al. (2014) find that, out of 11 systems with *Herschel*-resolved disks and well-measured stellar inclinations, all are consistent with being coplanar. Watson et al. (2011) measure the rotational axes of stars with resolved debris disks, and reach the same conclusion. Studies of *Kepler*-discovered multi-planet systems (Sanchis-Ojeda et al. 2012; Hirano et al. 2012; Albrecht et al. 2013; Chaplin et al. 2013) also have found that the orbital planes of the planetary systems tend to be well-aligned with the equators of the host stars. We believe these studies provide ample evidence that compact, low-mass planetary systems like τ Ceti are usually well-aligned systems.

Greaves et al. (2004) used the low rotational velocity measured by Saar & Osten (1997) as evidence that we are viewing τ Ceti within 40° of pole-on, which was inconsistent with their measurements of the disk inclination. However, at the SCUBA resolution and wavelength, background confusion made it difficult to measure the disk inclination. The analysis of the *Herschel* images presented here has made it clear that the disk is close to face-on, consistent with being aligned with the equatorial plane of τ Ceti.

Assuming the best-fitting inclination for the disk ($\sim 30^\circ$) equals the inclination for τ Ceti and its planetary system, the best-fit values of $M \sin i$ given in Tuomi et al. (2013) should be doubled. As found in Section 4.2.1 below, such masses still allow a dynamically stable configuration for the planets. Table 4 gives the masses, semima-

jor axes, and eccentricities for this system. We note that, however, this is only one possible configuration of planets that satisfies both the requirement of long-term stability and the Bayesian analysis of Tuomi et al. (2013).

4.2 Dynamical Simulations

We perform numerical simulations using `swift-rmvs4` (Levison & Duncan 1994), with a timestep of 0.002 years (0.73 days). This allows >15 timesteps per orbit for accurate calculation of the positions of all five planets, including the innermost planet, with an orbital period of only 14 days. All of our simulations were carried out on the Canadian Advanced Network for Astronomical Research (CANFAR; Gaudet et al. 2009).

For our dynamical simulations, we ignore the mass of the disk since the largest reasonable estimate of τ Ceti’s disk mass is about 10% of the mass of the outermost planet ($M_{\text{disk}} \simeq 1M_{\oplus}$; Greaves et al. 2004). While Moore & Quillen (2013) find that a disk mass this high relative to the planet masses can affect the dynamical stability lifetime of a planetary system, the system they modelled (HR 8799) extends to much larger separations from the star than that of τ Ceti. HR 8799b, the outermost planet in the system, has a semimajor axis of 68 AU (Marois et al. 2008) and the planetesimal disk extends from 100-310 AU (Matthews et al. 2014). If the HR 8799 system is scaled down so that the orbit of HR 8799b matches the outermost planet in the τ Ceti system, HR 8799’s entire debris disk would extend to only ~ 3 -6 AU, while in reality, τ Ceti’s disk mass is actually spread out to ~ 55 AU. Given the small semimajor axes of all the planets in the τ Ceti system, we therefore believe the contribution of the disk mass to the stability of the system is negligible.

We performed two types of simulations: planetary system stability and disk orbit stability. Planet stability simulations were run for 100 Myr, corresponding to over two billion orbits of the innermost planet, while disk simulations were run for 10 Myr with many massless test particles included in addition to the five planets to diagnose stable orbits for small bodies. Planetary systems were deemed unstable if any planet’s semimajor axis changes by $> 1\%$ over the course of an integration. The same change in semimajor axis is used to diagnose stable versus unstable disk particle orbits.

Given the infinite range of possible starting conditions for this multiplanet system, we chose a few representative possibilities and investigated the stability of those before proceeding to disk simulations. We found the highest eccentricities allowed by the statistical analysis of Tuomi et al. (2013) yielded unstable planetary systems. The more moderate (best-fit) eccentricities and very low eccentricities result in planetary systems stable on timescales of 100 Myr, even when planet masses are increased by a factor of $1/\sin i_{\text{sys}}$, up to inclinations out of the sky plane as low as 5° , nearly perpendicular to our line-of-sight.

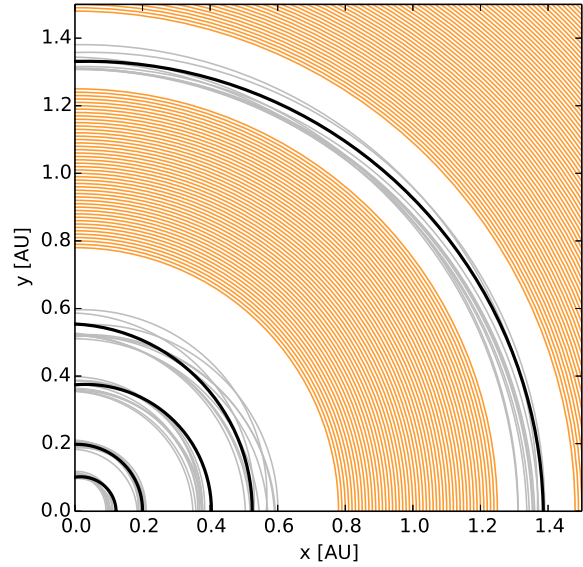


Figure 8. Initial (coplanar) orbits of 5 planets are shown in black, using masses and orbital elements as given in Table 4. Orbital elements which were unconstrained by the Tuomi et al. (2013) analysis (Ω , ω , and \mathcal{M}) are chosen at random. Gray lines show how the orbits evolve over the course of a 100 Myr integration. Stable disk particle orbits (surviving a 10 Myr integration) are shown in orange.

4.2.1 Disk Simulations

After confirming that the planetary system is stable over a reasonable range of possible orbital configurations, we use one stable planetary system (Table 4) as part of another set of simulations. Here we quantify the stability of small body orbits near planets in order to find where the debris disk would be stable over long timescales. The small bodies are represented by massless test particles in these simulations.

The fairly small planets of the τ Ceti system are on close-to-circular orbits and so they do not clear large annuli. Using just the best-fit parameters of the five planets from Tuomi et al. (2013) results in stable disk particle orbits all the way down to 0.1 AU separation from the orbit of the outermost planet (at 1.35 AU). Figure 8 shows that stable disk orbits also exist in the gap between the outermost two planets.

4.2.2 Simulations with an Additional Planet

One way to constrain the inner disk edge at greater distances from the star is to assume that there is an additional planet in the system further from the host star and to estimate the properties of this hypothetical companion based on the available data. Although this scenario was not specifically tested in the work of Tuomi et al. (2013), the radial velocity data sets could not be expected to be very sensitive to planets with masses of roughly that of Neptune on longer period (>5 yr) orbits.

In Figure 9, we show the estimated detection thresh-

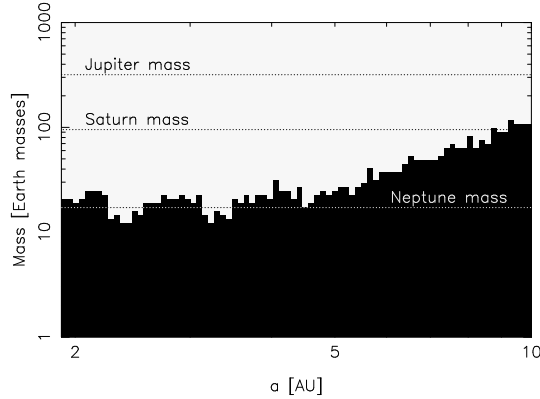


Figure 9. Black region shows planet mass (with the $\sim 30^\circ$ system inclination taken into account) and semimajor axis combinations that would not be detectable using the analysis methods of Tuomi et al. (2013). White region shows mass-semimajor axis combinations which cannot exist in the τ Ceti system based on current RV data.

old of additional planets orbiting the star based on the radial velocity data analysis of Tuomi et al. (2013). The area in the mass-period space where additional planet candidates are ruled out (white area) has been estimated by assuming there is an additional planet with a semimajor axis in excess of those of the previously proposed candidates. This estimation was performed by drawing a sample from the posterior probability density of the parameters of the sixth planet in a model that extends in the semi-major axis space from a minimum of 1.8 AU to a maximum value that we have chosen to be 10 AU, the outermost bound of the inner disk edge consistent with the *Herschel* data. The computations are performed as in Tuomi et al. (2014), and we have assumed that the planetary eccentricity has a prior probability density that penalizes high eccentricities as they approach unity, because the eccentricities of low-mass planets appear to follow such a distribution (Tuomi & Anglada-Escudé 2013).

It is worth noting that Jupiter-mass planets within 10 AU would have already been detected by previous RV studies (e.g. Pepe et al. 2011, see also analysis by Cumming et al. 2008). Using the analysis described above, Figure 9 shows that we can push to lower planetary masses, ruling out the existence of planets of Neptune-mass or larger within orbital distances of 5 AU, and excluding the possibility that Saturn-mass or larger planets exist in the system inside 10 AU.

We ran simulations with a sixth planet having twice Neptune’s mass on circular orbits at 5–10 AU, and find that these systems are stable on long timescales (100 Myr).

While the disk could be cleared to large semimajor axes by a more eccentric outer planet orbit, this situation would destabilize the inner five planets within millions of years at most. Using a circular orbit for the outermost planet constrains the stable disk particle orbits to just outside a few times the planet’s Hill radius, as expected. While it is exciting to consider the possibility of additional planets in the system, an additional planet with less than a Saturn mass (outside 5 AU) or less than a Neptune mass (inside 5 AU) would constrain the inner

edge of the disk to larger distances from the star. With the large uncertainties on inner edge of the disk, however, this additional layer of complexity is unwarranted. Future high-resolution images of the inner edge of τ Ceti’s disk will provide much-needed constraints on the actual location of the inner disk edge, and continued radial velocity observations may detect additional, more distant planets.

5 DISCUSSION

5.1 Properties of the τ Ceti Disk

Herschel observations have confirmed the existence of the resolved debris disk originally imaged by Greaves et al. (2004), though the inclination we measure is $\sim 30^\circ$ from face-on, which is different than the nearly edge-on alignment first reported from analysis of the SCUBA images. Modelling the disk gives some weak constraints on the extent of the disk, which extends roughly 2–55 AU from τ Ceti. There is no significant structure observed in the disk, and using a realistic dust grain spectrum (as opposed to blackbody) provided only moderately better constraints on the inner edge of the disk. Additional photometric or spectral data at far-IR wavelengths would be valuable for constraining dust grain properties in this system.

5.2 Disk Inner Edge

The current data do not constrain the inner disk edge very strongly. While an inner edge at 2–3 AU is consistent with both the SED- and image-based models, neither can formally rule out a disk extending as close to the star as 1 AU, well into the realm which may be populated by planets, or as far from the star as 10 AU, allowing dynamical room for one or more additional planets.

We note that interferometric near-IR measurements have been made of the τ Ceti system using the CHARA array (di Folco et al. 2007). They found they could reproduce the near-IR excess using a population of small ($< 1 \mu\text{m}$) dust grains extending from the limits of their observation field to extremely close to the star (3 AU to ~ 0.1 AU), which overlaps with the region where the planets may exist. However, the mass in dust grains is extremely small ($\sim 10^{-9} M_\oplus$), comparable to the mass of zodiacal (asteroidal) dust in our Solar System (Hahn et al. 2002). Models show that dust produced by collisions at larger distances can inspiral (due to Poynting-Robertson drag) past planets in the inner solar system with little disruption other than longer time spent inside planetary mean-motion resonances (Nesvorný et al. 2011). For this reason, the presence of this tenuous dust in the inner portions of the τ Ceti system does not rule out the planets.

The exquisite resolving power of ALMA should be able to image the inner edge of the main dust belt easily, and that will clarify which of three possibilities is true:

- 1) The disk extends well into the planetary regime (< 1.35 AU), which would be serious evidence against the planets proposed by Tuomi et al. (2013).
- 2) The disk edge is close to the orbit of the outermost

planet (>1.35 AU and <2.0 AU) and the proposed five planet system is enough to constrain the disk edge.

3) The disk edge ends significantly far away from the outermost planet (>2.0 AU), in which case another process must be invoked to explain the edge (e.g., another planet, or possibly collisional processes).

ALMA will also be more sensitive to larger dust grains that more closely trace the positions of the parent bodies that are collisionally grinding to make the smaller dust grains observed at mid- and far-IR wavelengths. The high-resolution of ALMA will also illuminate whether the dust in the τ Ceti debris annulus is produced by a narrow “birth ring” as has been observed in other debris disk systems (e.g. AU Mic; Wilner et al. 2012; MacGregor et al. 2013).

5.3 The Disk-Planet Relationship

If confirmed, τ Ceti’s low-mass multiplanet system would fit with the results of simulations by Raymond et al. (2011) and extend the trend observed by Wyatt et al. (2012): the presence of exclusively low-mass planetary systems ($< M_{\text{Saturn}}$) and far-IR excess ($\sim 70 \mu\text{m}$) is strongly correlated for mature host stars.

These models hint that systems with planets of mass $> M_{\text{Jup}}$ are inherently unstable in their early days (e.g. Raymond et al. 2012). We know from the structure of the Kuiper Belt that the four giant planets in our own Solar System have migrated, and that a much more massive primordial Kuiper Belt is required to fuel this migration (e.g. Gomes et al. 2005). It may be that the debris disk around solar analogue τ Ceti is brighter and more massive than the Kuiper Belt because there are no giant planets in the system to migrate and disrupt the primordial planetesimal disk.

Unfortunately, the *Herschel* images do not provide very tight constraints on the presence of gaps or clumps in the disk that may be due to perturbations by massive planets.

Resonant and secular perturbations by a planet on a disk can produce telltale clumps and gaps in the dust disk, but the grain sizes that are most visible at $70 \mu\text{m}$ and $160 \mu\text{m}$ will be smeared out by radiation forces relative to the larger (\sim millimeter-sized) dust grains and parent planetesimals, making these clumps much harder or even impossible to detect (Wyatt 2006). In addition, predicting clumps that may be present in the τ Ceti disk via numerical modelling of secular perturbations and mean-motion resonances in the planetesimal disk by the planets is not currently feasible. These perturbations are quite sensitive to the masses and exact orbits of the planets, which have very large uncertainties or are even completely unconstrained, as in the case of the angular orbital elements.

As shown in Section 3.1.1, the *Herschel* images are best reproduced using a smooth disk model, with no structure. However, because of the large beam size, this is not a very strong constraint on the smoothness of the disk. A several AU-wide gap could easily be missed due to the *Herschel* resolution. In order for a clump in the disk to be detectable, it would have to contain more than

$\sim 10\%$ of the total disk flux, based the sensitivities quoted in Table 2.

In order to rule out clumps or gaps in the disk with any degree of certainty, high-resolution, long wavelength observations are required in order to probe the distribution of large dust grains that are relatively unaffected by radiation forces. Within the next few months, ALMA observations will be used to probe the inner portions of the τ Ceti disk and provide some constraints both on the location of the inner edge of the disk and on the smoothness of the disk, which in turn will provide limits on the mass and orbital properties of undetected massive planets in the system, independent of the RV data.

6 SUMMARY AND CONCLUSIONS

τ Ceti hosts a bright debris disk that has been resolved by *Herschel*. The disk is uniform and symmetric, with a most likely inner edge at 2-3 AU (though inner edges 1-10 AU are not ruled out by the *Herschel* data) and an outer edge at 55 ± 10 AU. It is inclined from face-on by $35^\circ \pm 10^\circ$ and can be fit by a surface density distribution of dust that increases linearly with distance from the star.

The proposed five planet system is not ruled out by the disk model, and our dynamical simulations show that this system is stable for moderate planetary eccentricities. If the outermost planet is what constrains the inner edge of the disk, the inner edge should be at ~ 1.5 AU. If there is an additional, as-yet undetected planet (which is possible if its mass is below that of Neptune), it could be constraining the inner disk radius farther away from the star.

It appears that there are no Jupiter-mass planets inside 10 AU in the τ Ceti system, so the comparison to our Solar System may not be so appropriate. If the proposed planets are real, the τ Ceti system is composed of small rocky planets close to the star with a disk extending from the inner solar system out to Kuiper Belt-like distances from the star, perhaps resembling our Solar System if the giant planets had failed to form and the primordial planetesimal disk had not been disrupted by planet migration. Future high resolution observations are required to constrain the edges of the disk, and to confirm the planetary system.

ACKNOWLEDGEMENTS

The authors thank an anonymous referee for providing helpful comments on this paper. S.M.L. and B.C.M. acknowledge an NSERC Discovery Accelerator Supplement which funded this work. This work was also supported by the European Union through ERC grant number 279973 (G.M.K.) M.B. acknowledges support from a FONDECYT Postdoctoral Fellowship, project no. 3140479.

REFERENCES

Albrecht S., Winn J. N., Marcy G. W., Howard A. W., Isaacson H., Johnson J. A., 2013, *ApJ*, 771, 11

- Aumann H. H., 1985, *PASP*, 97, 885
 Bessel M. S., 1990, *A&AS*, 83, 357
 Booth M. et al., 2013, *MNRAS*, 428, 1263
 Chaplin W. J. et al., 2013, *ApJ*, 766, 101
 Chen C. H. et al., 2006, *ApJS*, 166, 351
 Cumming, A., et al. 2008, *PASP*, 120, 531
 Cutri R. M. et al., 2003, 2MASS All Sky Catalog of point sources.
 di Folco E. et al., 2007, *A&A*, 475, 243
 Dohnanyi J. S., 1969, *J. Geophys. Res.*, 74, 2531
 Gaudet S., Dowler P., Goliath S., Hill N., Kavelaars J. J., Peddle M., Pritchett C., Schade D., 2009, in D.A. Bohlender, D. Durand, P. Dowler, eds, *Astronomical Data Analysis Software and Systems XVIII. Astronomical Society of the Pacific Conference Series*, Vol. 411, p. 185
 Gomes R., Levison H. F., Tsiganis K., Morbidelli A., 2005, *Nature*, 435, 466
 Greaves J. S., Wyatt M. C., Holland W. S., Dent W. R. F., 2004, *MNRAS*, 351, L54
 Greaves J. S. et al., 2014, *MNRAS*, 438, L31
 Griffin M. J. et al., 2010, *A&A*, 518, L3
 Habing H. J. et al., 2001, *A&A*, 365, 545
 Hahn J. M., Zook H. A., Cooper B., Sunkara B., 2002, *Icarus*, 158, 360
 Hauck B., Mermilliod M., 1998, *A&AS*, 129, 431
 Hirano T. et al., 2012, *ApJ*, 759, L36
 Høg E. et al., 2000, *A&A*, 355, L27
 Holland W. S. et al., 1999, *MNRAS*, 303, 659
 Holmes E. K., Butner H. M., Fajardo-Acosta S. B., Rebull L. M., 2003, *AJ*, 125, 3334
 Ishihara D. et al., 2010, *A&A*, 514, A1
 Kennedy G. M., Wyatt M. C., Sibthorpe B., Phillips N. M., Matthews B. C., Greaves J. S., 2012, *MNRAS*, 426, 2115
 Kennedy G. M., Wyatt M. C., Bryden G., Wittenmyer R., Sibthorpe B., 2013, *MNRAS*, 436, 898
 Lagrange A. M. et al., 2010, *Science*, 329, 57
 Levison H. F., Duncan M. J., 1994, *Icarus*, 108, 18
 Li A., Greenberg J. M., 1997, *A&A*, 323, 566
 MacGregor M. A. et al., 2013, *ApJ*, 762, L21
 Mamajek E. E., Hillenbrand L. A., 2008, *ApJ*, 687, 1264
 Marois C., Macintosh B., Barman T., Zuckerman B., Song I., Patience J., Lafrenière D., Doyon R., 2008, *Science*, 322, 1348
 Matthews B., Kennedy G., Sibthorpe B., Booth M., Wyatt M., Broekhoven-Fiene H., Macintosh B., Marois C., 2014, *ApJ*, 780, 97
 Mermilliod J. C., 2006, *VizieR Online Data Catalog*, 2168, 0
 Moore A., Quillen A. C., 2013, *MNRAS*, 430, 320
 Moshir M. e., 1990, in *IRAS Faint Source Catalogue*, version 2.0 (1990). p. 0
 Mouillet D., Larwood J. D., Papaloizou J. C. B., Lagrange A. M., 1997, *MNRAS*, 292, 896
 Müller T., Nielbock M., Balog Z., Klaas U., Vilenius E., 2011, *PACS Observers Manual*, 708, 1728
 Nesvorný D., Janches D., Vokrouhlický D., Pokorný P., Bottke W. F., Jenniskens P., 2011, *ApJ*, 743, 129
 Ott S., 2010, in Y. Mizumoto, K.I. Morita, M. Ohishi, eds, *Astronomical Data Analysis Software and Systems XIX. Astronomical Society of the Pacific Conference Series*, Vol. 434, p. 139
 Pepe F. et al., 2011, *A&A*, 534, A58
 Perryman M. A. C., ESA, eds, 1997, *The HIPPARCOS and TYCHO catalogues. Astrometric and photometric star catalogues derived from the ESA HIPPARCOS Space Astrometry Mission*, ESA Special Publication, Vol. 1200
 Pilbratt G. L. et al., 2010, *A&A*, 518, L1
 Poglitsch A. et al., 2010, *A&A*, 518, L2
 Raymond S. N. et al., 2011, *A&A*, 530, A62
 Raymond S. N. et al., 2012, *ArXiv e-prints*
 Saar S. H., Osten R. A., 1997, *MNRAS*, 284, 803
 Sanchis-Ojeda R. et al., 2012, *Nature*, 487, 449
 Skrutskie M. F. et al., 2006, *AJ*, 131, 1163
 Spiegel D. S., Burrows A., 2012, *ApJ*, 745, 174
 Swinyard B. M. et al., 2010, *A&A*, 518, L4
 Tuomi M., Anglada-Escudé G., 2013, *A&A*, 556, A111
 Tuomi M., Jones H. R. A., Barnes J. R., Anglada-Escudé G., Jenkins J. S., 2014, *ArXiv e-prints*
 Tuomi M. et al., 2013, *A&A*, 551, A79
 van Leeuwen F., 2007, *A&A*, 474, 653
 Vandenbussche B. et al., 2010, *A&A*, 518, L133
 Watson C. A., Littlefair S. P., Diamond C., Collier Cameron A., Fitzsimmons A., Simpson E., Moulds V., Pollacco D., 2011, *MNRAS*, 413, L71
 Wilner D. J., Andrews S. M., MacGregor M. A., Hughes A. M., 2012, *ApJ*, 749, L27
 Wyatt M. C., Dent W. R. F., 2002, *MNRAS*, 334, 589
 Wyatt, M. C. 2006, *ApJ*, 639, 1153
 Wyatt M. C. et al., 2012, *MNRAS*, 424, 1206